Quaternary Science Reviews 356 (2025) 109286

Contents lists available at ScienceDirect

Quaternary Science Reviews

journal homepage: www.elsevier.com/locate/quascirev

Mid-Holocene hydroclimatic optimum recorded in a stalagmite from Shalaii Cave, northern Iraq

Dominik Fleitmann [a,*], Matthew Bosomworth [b], Diary Ali Mohammed Amin Al-Manmi [c], Melanie J. Leng [d,e], Diana Sahy [d], Karen Radner [f], Alistair Morgan [a], Alistair W.G. Pike [g], Mark Altaweel [h]

[a] *Department of Environmental Sciences, University of Basel, Basel, Switzerland*
[b] *Department of Archaeology, University of Reading, Reading, UK*
[c] *Department of Geology, College of Science, University of Sulaimani, Iraq*
[d] *National Environmental Isotope Facility, British Geological Survey, Keyworth, UK*
[e] *School of Biosciences, University of Nottingham, Loughborough, UK*
[f] *Department of History, Ludwig Maximilian University Munich, Munich, Germany*
[g] *Department of Archaeology, University of Southampton, UK*
[h] *Institute of Archaeology, University College London, London, UK*

ARTICLE INFO

Handling Editor: Mira Matthews

ABSTRACT

In Mesopotamia, climate is regarded as an important contributing factor to major socio-cultural transformations. However, the scarcity of Holocene paleoclimate reconstructions in this region impedes analysis of potential climate-human interactions. Furthermore, current hydroclimatic scenarios for Mesopotamia are predominantly based on oxygen isotope ($\delta^{18}O$) proxy records from the eastern Mediterranean, whereas the paleoclimatic significance of $\delta^{18}O$ remains debated. Here, we present a Holocene stalagmite multi-proxy record from Shalaii Cave in northern Mesopotamia. Based on stable isotope, trace element and strontium isotope measurements, our new Shalaii Cave record suggests that long-term changes in $\delta^{18}O$ were influenced by multiple factors, such as $\delta^{18}O$ changes of the source of moisture, amount and seasonality of rainfall. The Shalaii Cave trace element and strontium isotope records indicate rather dry conditions during the early Holocene and wettest conditions during the mid-Holocene. This mid-Holocene hydroclimate optimum at Shalaii Cave is in good agreement with other non-isotopic records from SW-Asia, such as pollen evidence for concurrent rapid forest expansion and peaking lake levels. The mid-Holocene hydroclimatic optimum is most likely related to an increase in the amount of spring precipitation related to the remote influence of the Indian summer monsoon (desert-monsoon mechanism) and spring insolation-driven weakening of the Arabian anticyclone. In particular the latter northward migration of the Arabian anticyclone in spring promoted a longer spring rainfall season.

1. Introduction

SW Asia is an key-region for paleoclimate research as the area is influenced by two major climate systems, the North Atlantic/Siberian pressure system and the Indian monsoon. The interaction between both systems remains highly uncertain due to the scarcity of paleoclimate records from this region. Furthermore, two of the most fundamental transformations in human history - the emergence of agriculture and first urban centres – took place between ~11,600 and 5000 years before present (yrs BP hereinafter). Considering the arid to semi-arid climate in this region, rainfall was an important contributing factor for both transformations. To date, the widely held view has been that rainfall peaked between approximately 11,600 and 6000 yrs BP and then decreased towards the present. This hydroclimate scenario forms the basis of many archaeological theories surrounding the development of agriculture and formation of urban centres (e.g., Lawrence et al., 2021). It is mainly based on calcite oxygen isotope records ($\delta^{18}O_{ca}$), which were obtained from several lakes and caves in SW-Asia (Fig. 1A). However, the interpretation of the $\delta^{18}O_{ca}$ records remains inconclusive as they are influenced by multiple factors, such as fluctuations in the amount of

---

* Corresponding author.
E-mail address: dominik.fleitmann@unibas.ch (D. Fleitmann).

https://doi.org/10.1016/j.quascirev.2025.109286
Received 30 July 2024; Received in revised form 28 February 2025; Accepted 1 March 2025

rainfall, long-term changes in the δ^{18}O of surface water in the Eastern Mediterranean (one of the main moisture sources of precipitation throughout SW Asia), shifts in the seasonality of rainfall and evaporation (Kolodny et al., 2005; Develle et al., 2010; Grant et al., 2012; Cheng et al., 2015; Rohling et al., 2015). Furthermore, the hydroclimatic scenarios derived from $\delta^{18}O_{ca}$ records contradict the delayed expansion of woodland in SW-Asia after ~6500 yrs BP (summarized by Djamali et al., 2010), also known as the "*Holocene precipitation paradox*" (Stevens et al., 2006; Jones et al., 2019). Moreover, most $\delta^{18}O_{ca}$ time series, such as the well-known and frequently cited Soreq Cave record (Bar-Matthews et al., 2003), are either located in the Levant (e.g., Cheng et al., 2015) and Turkey (Roberts et al., 2011; Finné et al., 2011), whereas records covering the entire Holocene are absent in many parts of SW-Asia and Mesopotamia, respectively (Fig. 1A). As a result, the hydroclimatic evolution across the Holocene remains poorly constrained, with some studies suggesting increasing aridity (Andrews et al., 2020; Roberts et al., 2011) and others higher precipitation since the mid-Holocene (Litt et al., 2012; Wick et al., 2003). Clearly, additional multiproxy hydroclimate proxy records are needed to reconcile the contrasting hydroclimate reconstructions in SW-Asia and to fill distinct spatial and temporal gaps in certain key-regions such as Mesopotamia.

Recently, studies from northern Iraq (northern Mesopotamia) revealed the high potential of speleothems for hydroclimatic reconstructions (Flohr et al., 2017; Marsh et al., 2018; Amin Al-Manmi et al., 2019; Sinha et al., 2019), but published reconstructions are relatively short and do not cover the entire Holocene period. Here, we present a new multi-proxy stalagmite record from Shalaii Cave in Iraqi-Kurdistan to disentangle the complex processes acting on terrestrial $\delta^{18}O_{ca}$ records and to present a revised long-term hydroclimatic framework for the Holocene period by providing more evidence for a mid-Holocene hydroclimate optimum in SW-Asia.

2. Environmental, climatic and cave settings

2.1. Modern climate and environment

SW Asia and Iraq respectively lie within a transition zone between major weather systems, including the North Atlantic, monsoonal and Siberian systems (e.g., Xoplaki et al., 2004). Climate in Iraq is therefore influenced by subtropical and mid-latitude processes and different air masses and these heterogenous interactions are further complicated by a complex topography and land-sea distribution. Present-day climate at Shalaii Cave is highly seasonal, with a wet autumn, winter and spring (October to May) and a dry and hot summer season (Fig. 2A). In winter, climate is dominated by mid-latitude westerlies storm tracks from the Mediterranean and North Atlantic (e.g., Barlow et al., 2016) and precipitation originates from eastward moving storm systems. Some of these storm systems can produce significant southerly fluxes of water vapour from the Persian Gulf during spring (Evans and Smith, 2006). Though the southerly dominated events are less common, they can contribute significantly to annual rainfall amounts in Iraq (deVries et al., 2016). In late spring, increasing heating of SW-Asia leads to the northward migration of the Arabian Anticyclone and thereby prevents the rain-bearing westerlies from reaching the area. Importantly, years with a shorter rainfall period are associated with an earlier northward movement of the Arabian anticyclone (Mohammadi et al., 2021). Intense subsidence of dry air over Iraq leads to hot and arid conditions in summer. The retreat of the Arabian Anticyclone in autumn allows the moist westerlies to reach the region again and marks the onset of the rainy season.

Precipitation is highly variable on interannual time scales (Fig. 2B) as indicated by meteorological stations throughout Iraq and Climate Research Unit (CRU) data (van Oldenborgh, 2016). Total rainfall, monitored at the nearby Chamchamal station, averages 460 mm yr^{-1} (2000–2014; Fig. 2B) and is mainly associated with eastward moving storm systems from the North Atlantic and Eastern Mediterranean,

Rainfall at Shalaii Cave is representative for a wider area, compromising almost all parts of the Eastern Fertile Crescent (EFC) (Fig. 1B). The correlation map reveals that conditions at Shalaii Cave correlate strongly (p-value >0.6) with variability observed across most of the EFC, and therefore speleothems from this cave are likely to provide suitable records to characterise conditions for the wider EFC.

2.2. Shalaii Cave and stalagmite SHC-03

Shalaii Cave (35.146°, 45.296°, 730 masl; Fig. 2) is a single entrance

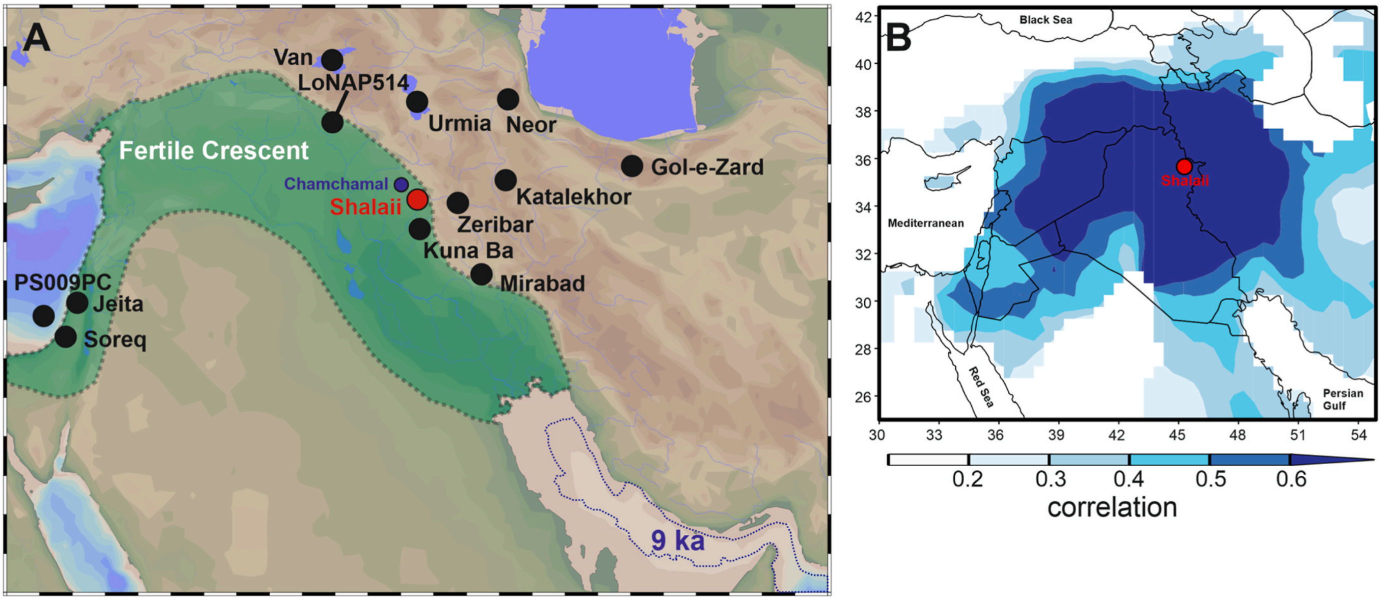

Fig. 1. **(A)** Location map with key-paleoclimate records from SW-Asia. Green shaded area marks the spatial extent of the Fertile Crescent. Blue dashed line denotes the coastline at around 9000 yrs BP (Lambeck, 1996). **(B)** Correlation map of rainfall variability between Shalaii Cave and other areas of SW Asia. Colors indicate the correlation of CRU TS4.06 precipitation data in the Shalaii Cave 0.5° grid cell with other areas in the Middle East. Map was generated in the KNMI Climate Explorer (van Oldenborgh, 2016). (For interpretation of the references to colour in this figure legend, the reader is referred to the Web version of this article.)

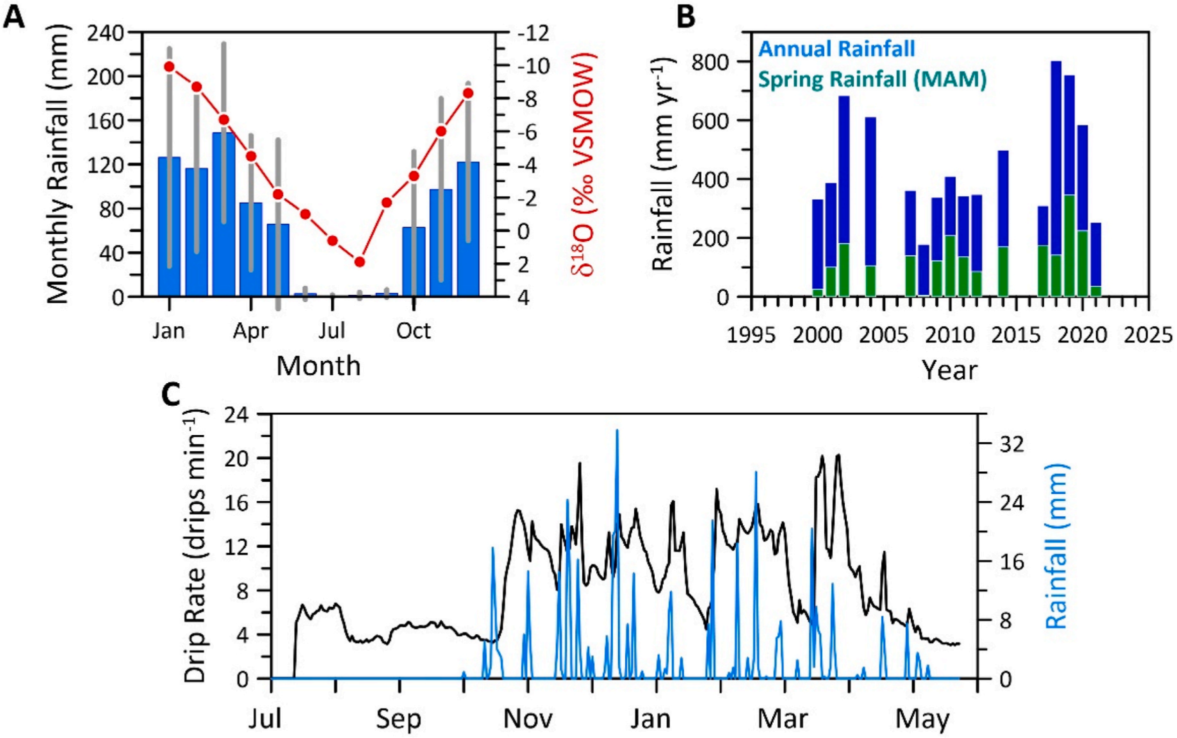

Fig. 2. **(A)** Monthly average of rainfall amount at Chamchamal station (~60 km from Shalai Cave; see also Fig. 1A) for 16 years with complete data (blue bars). Grey lines denote standard deviation. Red dotted line shows the oxygen isotopic of precipitation, calculated using the Online Isotopes in Precipitation Calculator (OIPC) (available from: https://wateriso.utah.edu/waterisotopes/pages/data_access/oipc.html; Bowen, 2020). **(B)** Annual mean (blue) and spring (March, April, May (MAM)) precipitation at Chamchamal station. Note that years with missing months are not shown. **(C)** Comparison between rainfall and Shalaii Cave drip rates for the period from June 2014 to May 2015. (For interpretation of the references to colour in this figure legend, the reader is referred to the Web version of this article.)

cave located in the Sangaw district, Sulaymaniyah province, Iraqi Kurdistan, in the foothills of the Zagros Mountains (Fig. 1A). Shalaii Cave is located on the southern tip of the Ashdagh (or Aj-Dagh) anticline and hosted within the middle Oligocene Bajawan (or Bajwan) formation, a highly jointed limestone that is partly dolomitised (Kharajiany, 2014). Due to the semi-arid climate conditions vegetation above the cave is sparse and is mainly composed of steppe shrubland and grasses. Soil thickness is relatively thin with substantial areas of exposed bedrock visible. The single-entrance cave is around 600 m long with the ceiling height reaching nearly 30 m and less than 1 m in small passages. Shalaii Cave is mostly horizontal, with some areas filled with sediments and collapsed rocks. There are two main galleries in the cave, a small gallery which is nealr 200 m away from the entrance and a large gallery 30 m further into the cave which contains abundant actively growing and fossil speleothems (Amin Al-Manmi et al., 2019). Cave air temperature at the sampling site of stalagmite SHC-03 is constant and averages 20.18 ± 0.01 °C, being very close to mean annual air temperature of 20.5 °C outside the cave. Relative humidity is 100 % and constant throughout the year in the deeper part of the cave where stalagmite SHC-3 was collected (Fig. 2). Drip rates monitored between 2014 and 2015 vary seasonally between 29,199 drips per day in winter to 4408 drips per day in summer (Amin Al-Manmi et al., 2019), indicating a relatively large storage capacity above the cave (Fig. 2C). The comparison between drip rates and amount of rainfall above the cave shows that aquifer recharge occurs during the rainy season, particularly in winter and spring. The average cave air $p\mathrm{CO}_2$ is 596 ppm. However, winter values were higher reaching 756 ppm and then falling to less than 484 ppm in mid–September, close to atmospheric levels. Seasonal variation in $p\mathrm{CO}_2$ is suggested to be the result of reversals in ventilation driven by temperature contrasts between the cave interior and exterior (Amin Al-Manmi et al., 2019). Drip rates were measured daily in Shalaii Cave between July 2014 and May 2015.

Stalagmite SHC-03 was sampled because it was one of the tallest stalagmites (3.17 m in height) in the cave, columnar shaped and also actively growing in the large chamber of Shalaii Cave (Supplementary Fig. S1). To get the stalagmite out of the cave, it was cut into thirteen slabs. The stalagmite fabric is composed of a creamy white porous calcite and dark brown semi-transparent mosaic calcite in the centre of SHC-03 (Fig. 3). SHC-03 has a clear hiatus visible at a depth of c.2,035 mm as a thick layer of recrystallised calcite and this has been verified by U-series dates (Supplementary Fig. S2).

3. Methods

3.1. Uranium-series dating

A total of 17 calcite samples for U-Th dates (Table 1) were collected and analysed in multiple stages between 2016 and 2019. The location of samples taken for U/Th dating are illustrated in Fig. 3A. U-series dating was done within a class 100 HEPA filtered clean lab at the National Environmental Isotope Facility, British Geological Survey, following a similar method to Crémière et al. (2016). Sample powders were weighed (228 mg–744 mg) and placed in Savillex vials, covered in MilliQ, and dissolved by drop-wise addition of 15 M HNO3 to ensure controlled and contained sample dissolutions. Samples were centrifuged and visually checked for complete dissolution and then spiked with a mixed high purity ^{229}Th/^{236}U tracer. The U-Th tracer was calibrated against gravimetric solutions prepared from CRM 112a U metal, Ames Laboratory high purity Th metal, and blank checked ~2.5 M HNO_3 + trace HF. The gravimetric solutions, tracer stock and tracer working solution are all stored in Nalgene FEP bottles that were rigorously cleaned before use with ultrapure acids for a minimum of 3 months. Spike-sample equilibration was achieved through drying the dissolved samples down, re-dissolution in 15 M HNO_3, and refluxing at ca. 100 °C for 24 h. All

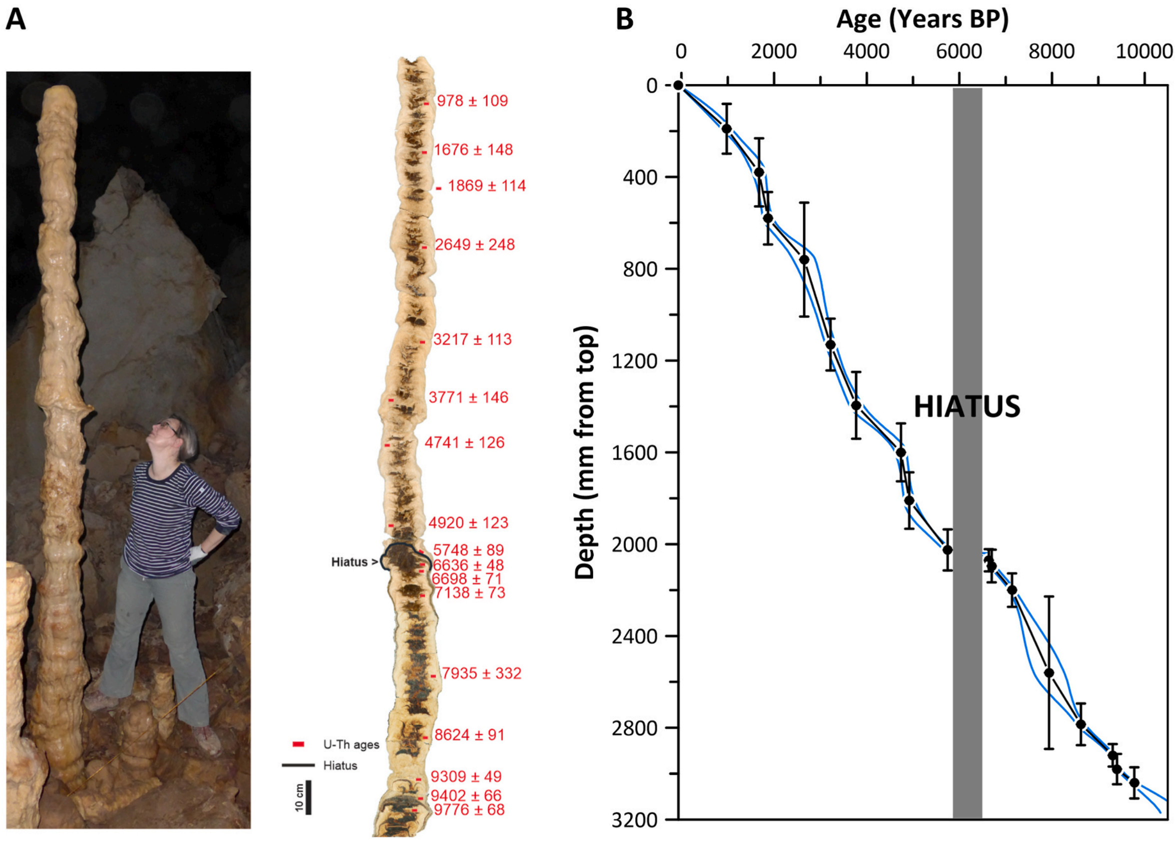

Fig. 3. **(A)** Images of stalagmite SHC-03 from Shalaii Cave. Cut and polished stalagmite with location of U-Th ages (red squares) and hiatus (black line). **(B)** Age model (black line) produced by COPRA for stalagmite SHC-03. Black circles are U-series dates used to produce the age model with their associated errors bars (2σ). Blue lines indicate the 95% confidence interval for the age model. (For interpretation of the references to colour in this figure legend, the reader is referred to the Web version of this article.)

samples went through two overnight oxidation steps in a mixture of 2 ml 16 M HNO_3 and 0.2 ml 30% H_2O_2 followed by evaporation to dryness. After oxidation the samples were dissolved in 1 M HCl, approximately 5 mg Fe as $FeCl_2$ was added, and U and Th pre-concentrated by Fe co-precipitation with ammonia. Initial separation on 0.6 ml columns using AG-1 × 8 anion exchange resin were done following the procedure of Edwards et al. (1987). Th fractions were further purified using a second pass through AG-1 × 8 resin and were filtered using 0.22-μm pore-size syringe filters to remove resin particles. Both U and Th fractions were oxidized twice in 2 ml 16 M HNO_3 and 0.2 ml 30% H_2O_2, and dissolved in 1 ml 0.1 M HCl and 0.035 M HF. Before mass spectrometry analyses, all samples were filtered to remove particles originating from the perfluoroalkoxy alkane (FEP) beakers used for sample preparation.

Isotope ratio measurements were made on a Thermo Neptune Plus MC-ICP-MS with samples introduced via an Aridus II desolvating nebulizer using an ESI PFA nebulizer tip with an ~50 μl/min uptake rate. Typical operating conditions included the addition of 4–8 ml/min high-purity N_2 to the sample-carrying Ar stream, to minimize U and Th oxide formation in the plasma. U measurements were made using a normal sample cone and X-skimmer cone, and a static multicollector data collection protocol with ^{234}U measured on an axial secondary electron multiplier (SEM), and ^{233}U, ^{235}U, ^{236}U and ^{238}U measured on Faraday cups equipped with 1011 Ω resistors. Blocks of five samples were bracketed by analyses of CRM 112a U and CRM 112a U + IRMM 3636. Exponential mass bias corrections were based on the measured values of the $^{233}U/^{236}U$ ratio of the IRMM 3636 spike normalized to a value of 1.01906. SEM/Faraday yield corrections were based on the $^{234}U/^{235}U$ ratio of bracketing unspiked CRM 112a analyses. Th measurements were made using X-skimmer and Jet sample cone using a static multicollector protocol with ^{230}Th measured on the axial SEM and ^{229}Th and ^{232}Th on Faraday cups. Blocks of ten samples were bracketed by blocks of five measurements of an in-house ^{229}Th-^{230}Th-^{232}Th reference solution to monitor mass bias and SEM/Faraday yield. Hydride formation and tailing were monitored at the beginning of each analytical session, with measurements made at mass 237 and 239, while aspirating an unspiked CRM 112a solution, and were corrected during offline data reduction.

U-Th age calculations were performed in Isoplot v. 3.75 Excel 2010 add-in (Ludwig, 2003). Activity ratios and ages were calculated using the decay constants of Cheng et al. (2013). Dates were corrected for detrital Th assuming an initial $[^{232}Th/^{238}U]$activity = 1.2 ± 0.6, $[^{234}U/^{238}U]$activity = 1.0 ± 0.5, and $[^{230}Th/^{238}U]$activity = 1.0 ± 0.5. Dates are reported in years BP, where the present is defined as the year 1950 CE.

3.2. *Stable isotope analysis*

A total of 1648 oxygen and carbon isotope ($\delta^{18}O$ and $\delta^{13}C$) measurements were performed on stalagmite SHC-03. Samples for $\delta^{18}O$ and $\delta^{13}C$ analysis were obtained by collecting calcite every ~2.5 mm through the stalagmite. This was done using a dremel hand drill. As a result of potential recrystallisation and complex growth structures in the central part of the stalagmite, samples were taken from a track adjacent to the central growth axis. These samples were analysed at the British Geological Survey. Approximately 60–100 μg of calcite were used for isotope analysis using an IsoPrime dual inlet mass spectrometer plus Multiprep device. Samples are loaded into glass vials and sealed with septa. The automated system evacuates vials and delivers anhydrous phosphoric acid to the calcite at 90 °C. The evolved CO_2 is collected for 15 min, cryogenically cleaned and passed to the mass spectrometer.

Table 1
Uranium-Thorium ages measured at the British Geological Survey.

Lab ID	Measured, Tracer-Corrected										Detrital-Corrected							
	Depth	U	^{232}Th	230/232 AR	232/238 AR	±2s	230/238 AR	±2s	234U/238U AR	±2s	230Th/238U AR	±2s	234U/238U AR	±2s	Age corr.	±2s	Int. 234U/238 U AR	±2s
	(mm)	(ppm)	(ppm)			(%)		(%)		(%)		(%)		(%)	(kyr BP)	(abs)		(abs)
143–16	190	0.09	0.001	6.5	0.002076	0.14	0.01355	1.23	1.2397	0.14	0.0118	10.36	1.2401	0.16	1.046	0.109	1.2408	0.002
143–17	380	0.11	0.001	7.8	0.002849	0.14	0.02217	1.14	1.2498	0.13	0.0198	8.46	1.2503	0.16	1.744	0.148	1.2516	0.002
143–18	580	0.09	0.001	10.9	0.002167	0.14	0.02370	1.06	1.2451	0.17	0.0219	5.85	1.2455	0.18	1.937	0.114	1.2468	0.002
137–3	760	0.10	0.001	7.2	0.004798	0.12	0.03463	0.49	1.2475	0.14	0.0308	9.05	1.2485	0.21	2.717	0.248	1.2504	0.003
137–4	1130	0.10	0.001	17.9	0.002147	0.12	0.03849	0.47	1.2372	0.14	0.0368	3.40	1.2377	0.16	3.285	0.113	1.2399	0.002
137–8	1395	0.11	0.001	16.2	0.002799	0.12	0.04534	0.42	1.2443	0.15	0.0431	3.75	1.2449	0.17	3.839	0.146	1.2475	0.002
143–19	1600	0.08	0.000	27.6	0.001997	0.15	0.05516	1.42	1.2401	0.14	0.0536	2.58	1.2405	0.16	4.809	0.126	1.2438	0.002
137–5	1810	0.10	0.001	24.7	0.002333	0.12	0.05754	0.44	1.2435	0.13	0.0557	2.42	1.244	0.15	4.988	0.123	1.2474	0.002
143–20	2025	0.08	0.000	50.9	0.001297	0.15	0.06608	0.97	1.2504	0.15	0.0651	1.50	1.2506	0.16	5.816	0.089	1.2548	0.002
152–14	2070	0.07	0.000	103.1	0.000729	0.04	0.07516	0.41	1.2483	0.17	0.0746	0.68	1.2485	0.17	6.705	0.048	1.2532	0.002
152–15	2095	0.09	0.000	61.8	0.00124	0.04	0.07656	0.44	1.2538	0.13	0.0756	1.02	1.2541	0.14	6.767	0.071	1.2590	0.002
152–16	2200	0.09	0.000	64	0.001289	0.04	0.08248	0.42	1.2713	0.12	0.0815	0.98	1.2716	0.13	7.207	0.073	1.2772	0.002
124–27	2560	0.12	0.002	14.8	0.006347	0.05	0.09371	0.75	1.2523	0.15	0.0889	4.05	1.2536	0.26	8.001	0.332	1.2594	0.003
143–24	2785	0.15	0.000	103.5	0.000949	0.14	0.09823	0.84	1.2693	0.14	0.0975	1.00	1.2695	0.14	8.692	0.091	1.2762	0.002
124–29	2920	0.17	0.000	254.8	0.000415	0.05	0.10564	0.44	1.2748	0.13	0.1053	0.49	1.2749	0.13	9.375	0.049	1.2823	0.002
137–7	2980	0.20	0.001	92.6	0.001164	0.12	0.10783	0.29	1.2819	0.13	0.1070	0.66	1.2822	0.13	9.470	0.066	1.2898	0.002
143–25	3040	0.16	0.000	118.4	0.000947	0.10	0.11217	0.46	1.2871	0.12	0.1115	0.65	1.2873	0.13	9.844	0.068	1.2954	0.002

Isotope values (δ^{13}C, δ^{18}O) are reported as per mill (‰) deviations of the isotopic ratios (^{13}C/^{12}C, ^{18}O/^{16}O) calculated to the VPDB scale using a within-run laboratory standard calibrated against NBS-19. The calcite-acid fractionation factor applied to the gas values is 1.00798. Due to the long run time of 21 h a drift correction is applied across the run when required, calculated using the standards that bracket the samples. The Craig correction is also applied to account for δ^{17}O. The average analytical reproducibility of the standard calcite (KCM) is 0.05‰ for δ^{13}C and δ^{18}O.

3.3. *Trace element analysis*

A total of 501 trace element (magnesium and strontium) were carried out at the School of Archaeology, Geography and Environmental Sciences (SAGES), University of Reading. 0.002g of powered calcite sample was diluted in 14.998g of ~2% trace element grade HNO3, resulting in a dilution factor of 7500. Samples were measured using PerkinElmer 7300 Dual View ICP-OES. Samples were nebulised using a Meinhard Type C nebuliser and introduced into the instrument using a cyclonic spray chamber. The plasma conditions were as follows: 15 L/min plasma gas flow, 0.2 L/min auxiliary gas flow, 0.4 L/min nebuliser gas flow, 1500W RF power and sample flow rate of 1 ml/min. All of the elements were measured radially, with the exception of Ba. The detection limits were 0.64 ppb for Ca, 0.04 ppb for Mg, <0.04 ppb for Sr, 0.01 ppb for Ba. RSD % for all elements were usually below 2%, all were below 5%. Final trace element data were converted from ppm to molarity and presented as a ratio to Ca (Tr/Ca) as a millimoles per mole (mmol/mol) value.

3.4. *Strontium isotope analysis*

A total of 95 strontium isotope (^{87}Sr/^{86}Sr) samples were undertaken to develop a multi-proxy record for stalagmite SHC-03. Initial ^{87}Sr/^{86}Sr analysis was conducted on 40 calcite samples (~15 mg) from stalagmite SHC-03 at the National Oceanography Centre, Southampton. These samples represented measurements every ~40 mm through the stalagmite before the main hiatus (Supplementary Fig. S2) and every ~130 mm during the latter half of the stalagmite after the hiatus.

For Sr separation with an ion-exchange resin column (0.2 mL Eichrom Sr resin), the NO_3^- concentration of sample solutions were adjusted to 3 M using 68% HNO_3. The resin column was pre-cleaned and conditioned with sub-boiled 3 M HNO_3. After loading the sample solution, 3-mL sub-boiled 3 M HNO_3 was added to the column to elute cations such as Ca, Ba and Rb. The Sr fraction was collected by adding 1.5-mL of ultra-pure H_2O. Procedural Sr blanks during the column separation procedure contained less than 0.6 ng Sr, which is insignificant for isotopic analysis using 1 μg Sr. Sr isotopic compositions were measured by thermal ionization mass spectrometer (Thermo-Finnigan Triton) using the rhenium single filament method with a tantalum oxide activator. ~1 μg of Sr in 1.0 μL solution was dried on an evaporation filament. During the measurement, the intensity of ^{88}Sr ion signal was maintained near 4×10^{11}A. The low ^{85}Rb signal ensured that the interference of ^{87}Rb on ^{87}Sr signal was insignificant (~0.1%) for all analyses. 150 cycles of data were acquired in a single run. Instrumental bias was corrected using NIST987 standard, which yielded an average ^{87}Sr/^{86}Sr value of 0.71024.

Following the first set of ^{87}Sr/^{86}Sr analysis, a second batch of calcite samples and a soil sample were collected for ^{87}Sr/^{86}Sr analysis. For this set of analysis another 50 calcite samples were collected to improve the temporal resolution of the latter half of the stalagmite. These were analysed at the ALS Scandinavia AB laboratory in Sweden. ^{87}Sr/^{86}Sr analysis was carried out after ion exchange separation as described above and prepared by closed vessel acid digestion. The samples were measured using an MC-ICP-MS (NEPTUNE Plus, ThermoScientific). An ^{87}Sr/^{86}Sr ratio of NIST SRM 987 of 0.71034 was used for instrumental mass bias correction.

To correct for inter-laboratory differences between the two different sets of analyses, the results of the second run were corrected by subtracting the difference between the average NIST SRM 987 value between the two laboratories.

4. Results and discussion

4.1. Chronology of stalagmite SHC-03

The age model of the 3.17 m tall stalagmite SHC-03 (Fig. 3A and B) is constrained by 17 Uranium-series ages (^{230}Th hereinafter), almost all of them are in stratigraphic order. However, age uncertainties are higher than usual due to relatively low Uranium concentrations of ∼0.1 ppm and detrital contamination. The age model for SHC-03 was constructed using COPRA (Constructing Proxy-Records from Age Model; Breitenbach et al., 2012). Based on the COPRA chronology, stalagmite SHC-03 grew almost continuously since ∼10,560 yrs BP (before present = before 1950 CE) except for a hiatus between ∼6640 and 5750 yrs BP (Fig. 3B). The hiatus is most likely not caused by climate, but rather due to a damage and loss of this section as a result of a major earthquake. Such damages are common in the region around Shalaii Cave, with the last major earthquake occurring in 2017 (https://www.bbc.co.uk/news/world-middle-east-41972338; accessed in March 2024). For instance, evidence for earthquake damage has been also found in a late Holocene stalagmite from Gejkar Cave (Flohr et al., 2017). The slight change in the growth direction across the hiatus is additional evidence for an earthquake (Supplementary Fig. S2). Because of the rather high chronological uncertainties, we focus on long-term trends and less on short-lived abrupt events, such as the 4.2 kyr event (Weiss et al., 1993). Stalagmite SHC-03 grew at a fairly constant growth rate of ∼0.33 mm yr^{-1}, similar to growth rates of between ∼0.27 mm yr^{-1} and ∼0.20 mm yr^{-1} in a stalagmite from nearby Gejkar Cave (Flohr et al., 2017).

4.2. Calcite oxygen and carbon isotopes in stalagmite SHC-03

Stalagmite SHC-03 $\delta^{18}O_{ca}$ values vary between −7.53 ‰ and −4.20 ‰ around a mean of −5.76 ‰ (Fig. 4A). $\delta^{18}O_{ca}$ values decrease abruptly between ∼10,560 and ∼10.280 yrs BP from around −6.11 to −6.93 ‰ and then decrease gradually from around −6.93 ‰–4.56 ‰ until ∼2200 yrs BP. Superimposed on the long-term trend are distinct decadal to multidecadal-scale fluctuations in $\delta^{18}O_{ca}$.

Several observations suggest that stalagmite SHC-03 was deposited under near isotopic equilibrium conditions. Firstly, the SHC-03 $\delta^{18}O_{ca}$ record is in very good agreement with contemporaneously deposited stalagmites from Shalaii Cave (Amin Al-Manmi et al., 2019) and Kuna-Ba Cave (Sinha et al., 2019) (Fig. 3A). Secondly, there is no statistically significant correlation between $\delta^{18}O_{ca}$ and $\delta^{13}C_{ca}$ ($r^2 = <0.01$). Thirdly, using the calculation of Tremaine et al. (2011), $\delta^{18}O$ values of modern drip water (11 samples were collected in 2014) in Shalaii Cave of around −5.49 ± 0.22 ‰ (VSMOW) and the measured cave air temperature of ∼20.2 °C, the calculated value of −5.62 ‰ are almost identical to the measured $\delta^{18}O_{ca}$ value of −5.32 ‰ at the top of stalagmite SHC-03. Based on these observations, stalagmite SHC-03 $\delta^{18}O_{ca}$ values should reflect the amount weighted isotopic composition of rainfall above Shalaii Cave. The SHC-03 $\delta^{18}O_{ca}$ profile is similar to other speleothem and lake oxygen and hydrogen isotope records from SW Asia

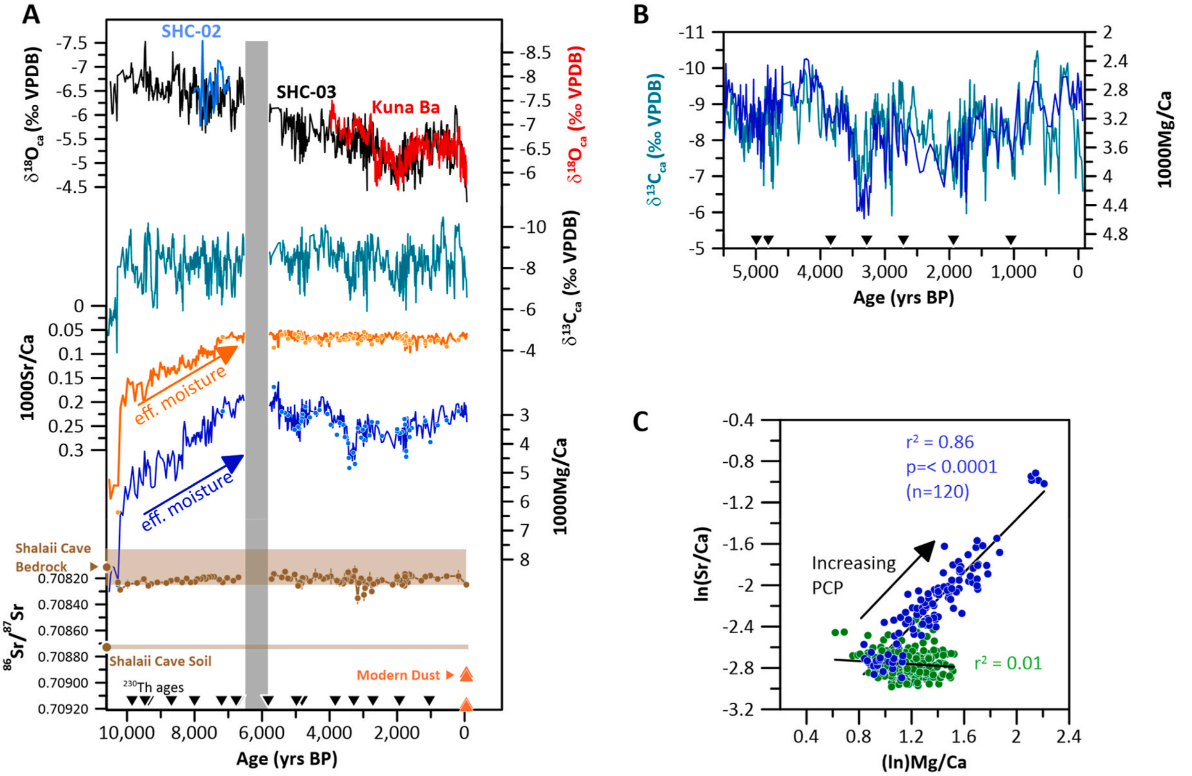

Fig. 4. **(A)** Multiproxy record from stalagmite SHC-03 from Shalaii Cave. The SHC-$\delta^{18}O_{ca}$ record (black line) in comparison to other isotope records from Iraqi-Kurdistan, including Kuna Ba (Sinha et al., 2019), Shalai Cave (Amin Al-Manmi et al., 2019). The SHC-03 $\delta^{13}C_{ca}$, Sr/Ca and Mg/Ca trace element records. Bright orange dots (Sr/Ca profile) and blue dots (Mg/Ca profile) indicate trace elements measurements of strontium isotope samples. $^{86}Sr/^{87}Sr$ measurements for stalagmite SHC-03 (brown circles), bedrock and soils above Shalaii Cave. The brownish area marks the isotopic range of bedrock and soils above the cave and. Orange triangles denote $^{86}Sr/^{87}Sr$ values of modern dust in Mesopotamia (Kunkelova et al., 2022). Black triangles mark Uranium-series ages. **(B)** Comparison between the SHC-03 $\delta^{13}C_{ca}$ and Mg/Ca trace element. **(C)** Correlation between ln(Mg/Ca) and ln(Sr/Ca). Blue circles are data point before the hiatus (10,560–6540 yrs BP) and green circles are data points after the hiatus (5780 yrs BP – present). (For interpretation of the references to colour in this figure legend, the reader is referred to the Web version of this article.)

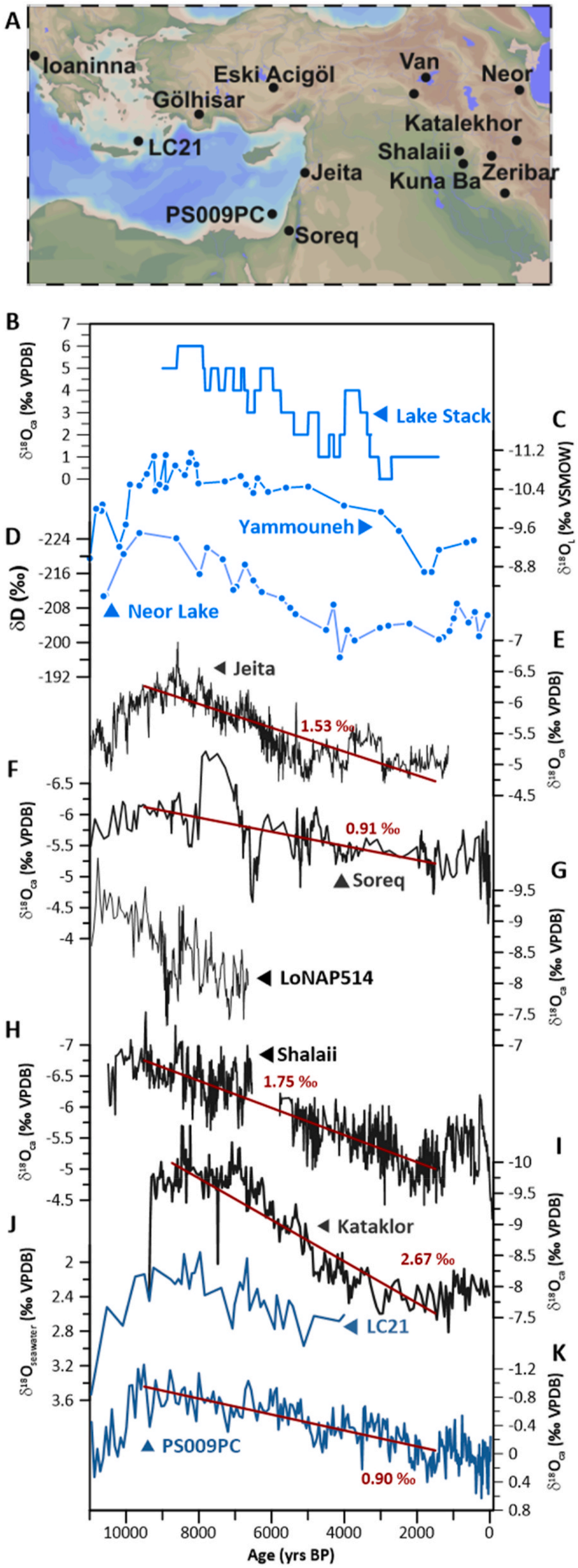

Fig. 5. Comparison of oxygen isotope records from the Eastern Mediterranean and SW Asia. **(A)** Map showing the location of isotope records. **(B)** Stacked lake record (based on 6 lakes from the EM and SW-Asia) (Roberts et al., 2011), **(C)** Yammouneh Lake (Develle et al., 2010) and **(D)** Neor Lake (Sharifi et al., 2015). **(E–I)** Speleothem $\delta^{18}O_{ca}$ records from **(E)** Jeita Cave (Cheng et al., 2015), **(F)** Soreq Cave (Bar Matthews et al., 2003), **(G)** LoNAP514 site (Regattieri et al., 2023), **(H)** Shalaii Cave (this study) and **(I)** Kataklor Cave (Andrews et al., 2020). **(J–K)** Marine $\delta^{18}O$ records from sediment cores LC-21 (Rohling et al., 2002) and PS009PC (Hennekam et al., 2015) from the Eastern Mediterranean.

(Fig. 5A–K), all of them display an early Holocene minimum and ong-term increase in $\delta^{18}O_{ca}$ towards the present.

Stalagmite SHC-03 $\delta^{13}C_{ca}$ values display a range from −10.48 to −3.88 ‰, varying around a mean of −8.23 ‰. Like the $\delta^{18}O_{ca}$ data, $\delta^{13}C_{ca}$ values are high in the lowermost part of stalagmite SHC-03 and the shift abruptly from lower values from −4.72‰ to −8.01‰ at ~10.280 yrs BP. After this shift, the $\delta^{13}C_{ca}$ profile remains remarkably stable for the remainder of the record, exhibiting no long-term trend and varying around a mean state of −8.28 ‰. However, larger variability of up to 4 ‰ is superimposed on the $\delta^{13}C_{ca}$ profile. In most speleothems from arid to semiarid environments, $\delta^{13}C_{ca}$ values are influenced by amount of precipitation as soil moisture is an important control for the type/density of vegetation and soil respiration rates (e.g., Cheng et al., 2015; Flohr et al., 2017). Furthermore, recharge conditions (open- and closed-system), prior calcite precipitation (PCP) and CO_2 degassing within the cave are additional factors modulating $\delta^{13}C_{ca}$ values (e.g., Fohlmeister et al., 2020). In general, $\delta^{13}C_{ca}$ values of −14 to −6‰ and −6 to 2‰ can be indicative of C3 and C4 vegetation respectively (e.g., McDermott, 2004). Carbon isotope values in stalagmite SHC-03 $\delta^{13}C$ values vary between −4.2 ‰ and −10.48 ‰ around a mean of −8.28 ‰ (Fig. 4B). $\delta^{13}C$ values ranging from around −4.2 ‰ to – 6.10 ‰ between ~10,560 and ~10,280 yrs BP are indicative of a C4 dominated vegetation above Shalaii Cave. A rapid change to a mixed C3/C4 vegetation and higher soil respiration rates at ~10,280 yrs BP is indicated by shift towards s more negative $\delta^{13}C_{ca}$ values of around −8.00‰. Since C4 vegetation is typically more drought and extreme temperature tolerant than C3 vegetation, the shift from a C4 to C3/C4 mixed landscape suggest a significant climate amelioration to warmer and wetter conditions. The shift is contemporary to similar trends observed in the $\delta^{18}O_{ca}$ and trace element data (Fig. 4A) that supports the interpretation that this is climate related. After this abrupt shift, $\delta^{13}C_{ca}$ values remain remarkably stable, varying around a mean value of −8.28 ‰ between ~10,280 years and today, indicating a mixed C3/C4 vegetation above the cave persisted until today. This interpretation is supported by the present-day shrub/grassland above the cave. The long-term stability of the SHC-03 $\delta^{13}C_{ca}$ record during the last ~10,280 years would suggest that the dominance of the vegetation type and density on the $\delta^{13}C_{ca}$ signal masks any other centennial – millennial trends in the $\delta^{13}C_{ca}$ data, somewhat limiting its use to observe longer term trends in moisture variability. However, multi-decadal fluctuations in $\delta^{13}C_{ca}$ are most likely related to variations in the amount of rainfall and drip rates within the Shalaii Cave, whereas reduced rainfall and lower drip rates enhance fractionation of $\delta^{13}C$ due to enhanced CO_2 degassing. Furthermore, vegetation density and soil respiration rates would be also reduced during more arid periods, which would reduce the contribution of biogenic soil CO_2 and result in a shift to higher carbon isotope values.

4.3. Magnesium and strontium contents in stalagmite SHC-03

Magnesium and Strontium contents show distinct changes across the Holocene period (Fig. 4A). Between 10,560 and ~10,260 yrs BP, both Mg/Ca and Sr/Ca values are at their highest of the entire SHC-03 record, averaging 8.58 and 0.38 resepctively during this time. After ~10,260, both Mg/Ca and Sr/Ca exhibit an abrupt shift to lower, but still relatively high, values corresponding to a similar shift in the SHC-03 isotope records (Fig. 4A). After this early part of the record, both Mg/Ca and Sr/Ca exhibit a long, steady trend towrd lower values until approximately the hiatus from 6.48 to 2.49 and 0.21 to 0.06 respectively. After the hiatus, the Mg/Ca data exibits a quasis "U-shaped" trend from low values at the end of the hiatis to higher values reached around 1800 yr BP before a shift toward lower values again, with centennial to decadal-scale variability superimposed on this long-term trend. The Sr/Ca remains constant throughout this later period and show only minor fluctuations around a mean of 0.06.

Magnesium and strontium contents in speleothems are known to be sensitive hydroclimate proxies as both are influenced by factors which are closely related to rainfall and/or effective moisture through prior calcite precipitation (PCP), water-rock interaction and incongruent calcite dissolution (ICD) and/or dust flux (e.g., Fairchild et al., 2006; Flohr et al., 2017; Carolin et al., 2018). Important for this study, all of these factors act in the "same direction" with respect to the amount of rainfall and recharge conditions above Shalaii Cave, that is lower rainfall and effective moisture lead to higher speleothem Mg/Ca due to reduced groundwater recharge, enhanced PCP, longer bedrock-water interaction (important for ICD) and/or enhanced dust flux above the cave.

Between ~10,560–~6540 yrs BP, we observe a strong correlation between ln(Mg/Ca) and ln(Sr/Ca) suggest PCP as the principal driver for varying Mg/Ca and Sr/Ca ratios between ~10,560–~6540 yrs BP (Fig. 4C). The correlation coefficient of $r^2 = 0.86$ ($p=<0.001$) and slope of 1.33 are strong indicators for PCP, whereas the slope is within the upper level of the range set out by Wassenburg et al. (2020).

Reduced rainfall would lead to reduced meteoric water recharge and lower water levels within the vadose zone, which in turn would promote enhanced PCP and higher Mg/Ca and Sr/Ca ratios in stalagmite SHC-03.

With the restart of growth at ~5780 yrs BP, correlation between Mg ad Sr is non-existent ($r^2 = -0.08$), suggesting that PCP is not the major driver of for trace element variations anymore, possibly as rainfall was generally higher. Rather, Mg/Ca ratios in stalagmite SHC-03 are most likely influenced by incongruent dissolution of dolomite and the different dissolution characteristics of calcite and dolomite related to changes in water-rock contact times. Generally, longer groundwater residence times during more arid climatic conditions would lead to a saturation of the water with respect to $CaCO_3$ and a higher contribution of Mg from the partially dolomitised bedrock (Bajawan Formation) to the drip water chemistry, which in turn results in higher Mg/Ca ratios in stalagmite SHC-03. This assumption is supported by the close correlation between Mg/Ca and $\delta^{13}C_{ca}$ on decadal to multi-decadal time scales (Fig. 4B), with lower $\delta^{13}C_{ca}$ values indicative of moister conditions, denser plant cover and enhanced soil microbial activity and higher drip rates (e.g., Flohr et al., 2017).

Higher Mg/Ca ratios, however, could be also related to enhanced deposition of dust above the cave which is subsequently leached into cave drip water (e.g., Goede et al., 1998; Frumkin and Stein, 2004; Carolin et al., 2018). This mechanism, however, is rather unlikely as episodes of major dust mobilization in the Middle East, such as between ~6500 and ~5000 yrs BP (Fig. 6) (Arz et al., 2003; Sharifi et al., 2015) do not coincide with elevated Mg/Ca ratios in stalagmite SHC-03. This is also supported by measured $^{87}Sr/^{86}Sr$ ratios in stalagmite SHC-03 (see paragraph 4.5 for further details), which suggest a stronger bedrock than soil and dust contribution to Sr.

4.4. Strontium isotopes in stalagmite SHC-03

Stalagmite SHC-03 $^{87}Sr/^{86}Sr$ ratios vary within a narrow range between 0.70814 ± 0.000035 and 0.70835 ± 0.000039 around a mean of ~0.70821, whereas a distinct trend across the Holocene is not detectable (Fig. 4A). $^{87}Sr/^{86}Sr$ ratios in speleothems are a direct proxy of the cave drip water and are often used as a proxy for dust input and/or bedrock water interaction in karst areas (e.g., Utida et al., 2020). At Shalaii Cave, strontium in cave drip waters and therefore speleothem calcite could derive from basically three sources: atmospheric dust, soil above the cave and/or the overlying limestone. $^{87}Sr/^{86}Sr$ ratios of two soil samples above Shalaii Cave is 0.70870 and three bedrock samples average 0.70811 (Fig. 4A). Soil $^{87}Sr/^{86}Sr$ ratios are very close to $^{87}Sr/^{86}Sr$ ratios of 0.70906 in four modern dust samples from Iraq (Sharifi et al., 2018; Kunkelova et al., 2022). Using the $^{87}Sr/^{86}Sr$ ratios of soil and bedrock samples from Shalaii Cave as endmembers, we can calculate the bedrock contribution (BC) to the SHC-03 signal using the equation (Utida et al., 2020):

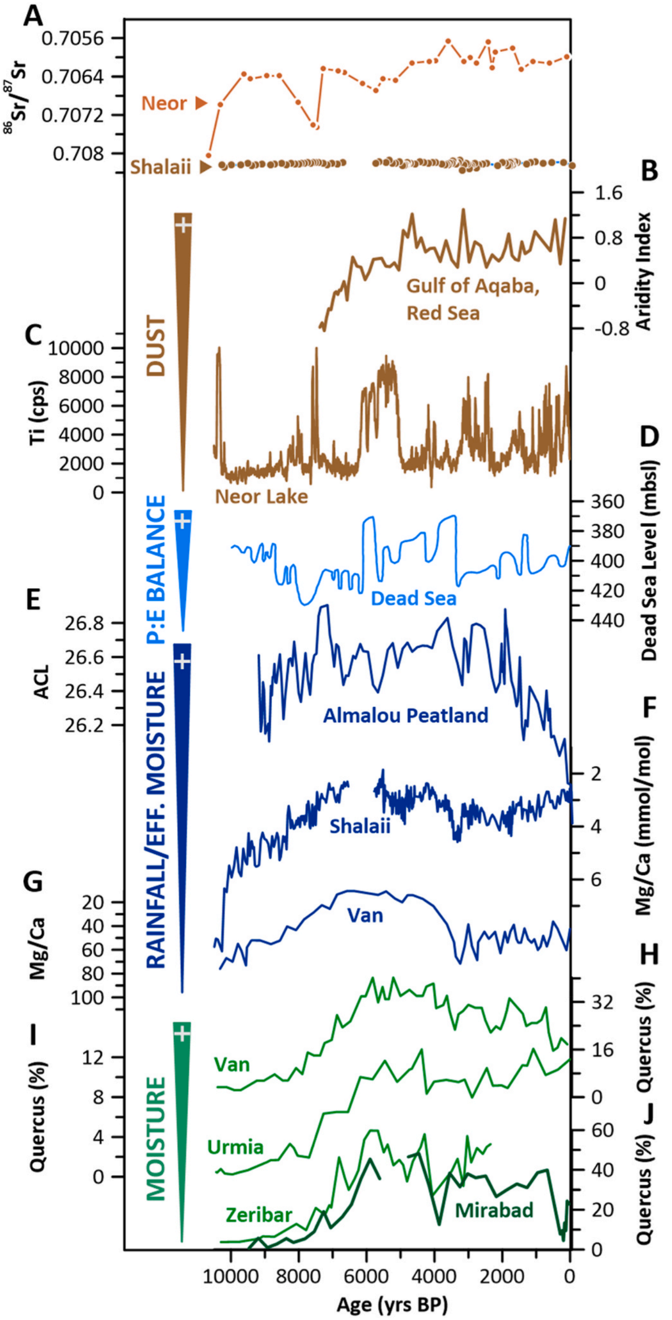

Fig. 6. Comparison of dust, hydroclimate and pollen records from SW Asia. (A) $^{86}Sr/^{87}Sr$ isotope profiles from Neor Lake (Sharifi et al., 2018). **(B)** Aridity index from the Gulf of Aquaba based on a sediment core GeoB 5804-4 from the northern Red Sea (Arz et al., 2003). **(C)** Titanium record from Neo Lake in Iran (Sharifi et al., 2015). **(D)** Dead Sea lake levels (Migowski et al., 2006). **(E)** Almalou Peatland ACL (average chain length) record (Chen et al., 2024). **(F–G)** Mg/Ca records from **(F)** Shalaii Cave (this study) and **(G)** Lake Van (Wick et al., 2003). **(H–J)** Quercus pollen records from Van (Wick et al., 2003), Zeribar(Stevens et al., 2006), Urmia (Stevens et al., 2012) and Mirabad (Stevens et al., 2006). (For interpretation of the references to colour in this figure legend, the reader is referred to the Web version of this article.)

$$BC = [(^{87}Sr/^{86}Sr_{speleo} - {}^{87}Sr/^{86}Sr_{soil}) / (^{87}Sr/^{86}Sr_{bedrock} - {}^{87}Sr/^{86}Sr_{soil})] \text{ x } 100$$

Based on the calculation above, BC values between 70 % and 95 % suggest that the limestone bedrock is the primary source of Sr (and Mg), with a minor soil and dust contribution. This supports our observations that Mg/Ca ratios in speleothem SHC-03 are not primarily governed by dust flux but rather by hydrologic processes in the epikarst and cave.

Furthermore, neither the Mg/Ca and ^{87}Sr/^{86}Sr records show any similarities to regional dust records from Neor Lake in Iran (Sharifi et al., 2015) or sediment core GeoB 5804-4 from the northern Red Sea (Arz et al., 2003). This is most evident during the early Holocene when SHC-03 Mg/Ca ratios are high and dust mobilization across the Middle East and SW Asia was reduced (Fig. 6). Likewise, the major increase in dust flux during the mid-Holocene in the Red Sea (core GeoB-885) and Iran (Neor Lake) neither coincides with a distinct increase in SHC-03 Mg/Ca nor significant shift in ^{87}Sr/^{86}Sr ratios (Fig. 6A–C). Overall, stalagmite SHC-03 ^{87}Sr/^{86}Sr values of ~0.7082 indicate an average host rock contribution of ~80% of Sr throughout the Holocene, indicating that fluctuating Mg/Ca ratios are influenced by PCP and/or ICD and, thus, to effective moisture and rainfall respectively. Furthermore, when compared to the continuous ^{87}Sr/^{86}Sr record from Neor Lake, which is influenced by dust flux, variations in SHC-03 ^{87}Sr/^{86}Sr ratios are considerably smaller. Overall, stalagmite SHC-03 ^{87}Sr/^{86}Sr isotopes provide further support that Mg/Ca ratios are not significantly influenced by dust deposition above Shalaii Cave.

5. The Holocene hydroclimate evolution in SW Asia

5.1. *Paleoclimatic significance of oxygen isotope values in speleothems from SW-Asia*

Our new Shalaii Cave multi-proxy record helps to disentangle the multiple influences contributing to the Holocene trend in speleothem-based $\delta^{18}O_{ca}$ records from SW-Asia, whereas the amount effect is just one of several factors (e.g., Kolodny et al., 2005; Develle et al., 2010; Cheng et al., 2015; Reuter et al., 2017; Chen et al., 2024). Additional factors include changes in the seasonal distribution of rainfall (e.g., Stevens et al., 2006), source effect (e.g., Bar-Matthews et al., 2003) and isotope fractionation effects in the soil zone, epikarst and cave (e.g., Flohr et al., 2017). Evaluating the influence of cave and air temperature changes on the SHC-03 $\delta^{18}O_{ca}$ record is very difficult due to the complete lack of quantitative paleotemperature estimates from this region. However, pollen-based temperature estimates from the south-east Europe indicate only minor variations of around ±1.2 °C in mean annual temperature (Davis et al., 2003). This is in agreement with simulated warmer mean annual temperatures of between 0.3 and 0.7 °C during the middle Holocene (Reuter et al., 2017). Since surface air temperature and δ^{18}O in precipitation are positively correlated, the so-called temperature effect is around 0.6 ‰/°C (Rozanski et al., 1992), slightly elevated mean annual air temperature would lead to slightly more positive δ^{18}O values in precipitation and stalagmite calcite during the middle Holocene. The comparison of δ^{18}O records from across SW-Asia shows similarities and differences in isotopic patterns, indicating changes in the relative influence of these factors on individual records.

The source effect is most likely an important factor and partly responsible for the long-term trend in δ^{18}O records (Fig. 5) and caused by changes in the isotopic composition of surface water in the Eastern Mediterranean. During the early and middle Holocene, the δ^{18}O of Eastern Mediterranean surface water was considerably lower because of the enhanced input of isotopically lighter freshwater along the North African margin (e.g., Nile discharge) and from the Black Sea and runoff around the basin. This freshwater input is well document by two marine records LC21 (Rohling et al., 2002; Marino et al., 2009) and PS009PC (Hennekam et al., 2015), both of them display their most negative $\delta^{18}O_{ca}$ values between ~10,500 and ~6100 yrs BP (Fig. 5J and K), concurrent with peak intensities of the African and Indian monsoons, the African Humid Period (deMenocal et al., 2000; Gasse, 2000; Fleitmann et al., 2003; Kuper and Kröpelin, 2006) and formation of sapropel S1 (e.g., Rohling et al., 2015) in the Eastern Mediterranean basin. Because the Eastern Mediterranean is a very important evaporative source for rainfall in the in SW Asia, lower δ^{18}O of sea surface water resulted in lower δ^{18}O of water vapour and rainfall during the early and middle Holocene. Such a strong sea-land oxygen isotopic relationship in the Eastern Mediterranean is well documented by numerous studies (e.g., Bar-Matthews et al., 2003; Almogi-Labin et al., 2009; Cheng et al., 2015) and was, for instance, used to transfer the chronology of the precisely dated Soreq Cave record to the Mediterranean sediment core LC21 by aligning the foraminifera-based δ^{18}O time series to the speleothem δ^{18}O record (Grant et al., 2012). Thus, the source effect accounts for a part of the long-term trend in downstream terrestrial $\delta^{18}O_{ca}$ records from SW-Asia (Fig. 5B–J), including the SHC-03 record (Kolodny et al., 2005; Develle et al., 2010; Cheng et al., 2015; Reuter et al., 2017). However, the source effect cannot account for the isotopic shift of ~1.75 ‰ between 9500 and 1500 yrs BP in the Shalaii Cave δ^{18}O record, as the isotopic change of seawater in the Eastern Mediterranean is only ~0.90 ‰ over the same time interval (Hennekam et al., 2015). Progressive isotopic shifts of between ~1.53 ‰ and ~2.67 ‰ in the Jeita and Kataklor Cave records are also significantly higher, (Fig. 5E–I), indicating that additional changes in seasonal distribution of rainfall above Shalaii Cave and the other cave sites could account for the larger isotope change in almost all speleothem δ^{18}O records from SW-Asia.

In the region of Shalaii Cave, δ^{18}O values of regional rainfall (Amin Al-Manmi et al., 2019) display a distinct seasonal pattern (Fig. 2A), whereas winter (DJF) rainfall is more negative in δ^{18}O compared to spring (MAM) and fall (SON) rainfall. A higher proportion of isotopically depleted winter precipitation during the early Holocene would therefore lead to a shift towards lower cave drip water and speleothem calcite δ^{18}O values and vice versa, even though total annual rainfall was not necessarily higher. The opposite behaviour between stalagmite SHC-03 Mg/Ca ratios and $\delta^{18}O_{ca}$ values during the early Holocene does not reconcile with the amount effect. If the amount effect would be the dominant control on $\delta^{18}O_{ca}$, then one would rather expect more negative $\delta^{18}O_{ca}$ values coinciding with lower Mg/Ca ratios (Fig. 4A). This is apparently not the case and it is therefore more plausible that a change from an early Holocene winter dominated to a mid-to late-Holocene winter/spring dominated rainfall regime occurred above Shalaii Cave. This climate scenario is also supported by Lake Zeribar, where paired δ^{18}O and Sr measurements on *C. neglecta* valves show more negative δ^{18}O values which coincide with elevated Sr/Ca molar values, the latter are indicative of higher lake water salinity and more arid conditions during the early Holocene (Stevens et al., 2001, 2006).

Taken all evidences together, the amount effect is most likely not the primary factor influencing speleothem $\delta^{18}O_{ca}$ records in northern Iraq and SW Asia; the source and seasonality effects are additional controls, which can counteract the amount effect. On orbital time scales, $\delta^{18}O_{ca}$ is a rather complex hydroclimate proxy that is influenced by multiple and non-stationary factors, i.e. the relative contributions of multiple effects exert variable influences on δ^{18}O in rainfall during the Holocene period. Our assumption is supported by a comprehensive comparison of lake and speleothem δ^{18}O records from the Middle East with an isotope-enabled climate model, which showed that more negative δ^{18}O values during the early and middle Holocene are caused by the combination of isotope drivers (Reuter et al., 2017). These include changes in the isotopic composition of vapour, precipitation amount, seasonality and local surface temperature. Thus, diverging isotopic patterns in some records could be explained by regional effects and changes in the relative influence of the aforementioned isotopic drivers in the individual records shown in Fig. 5.

5.2. *Evidence for the mid-Holocene hydroclimate optimum in SW-Asia*

Considering the uncertainties surrounding the interpretation of speleothem and lake $\delta^{18}O_{ca}$ records, non-isotope proxy records are most likely better suited to describe the long-term Holocene hydroclimate evolution in the SW Asia. Taking stalagmite SHC-03 Mg/Ca ratios as proxy for effective moisture and aquifer recharge, the Holocene hydroclimate optimum lasted from ~7000 to 4000 yrs BP (Fig. 6F), a timing that is in good agreement with several other non-isotopic records from SW-Asia (Fig. 6B–J). For instance, several pollen records from the Zagros-Taurus mountains show maximum expansion of deciduous oak woodland after ~6500 yrs BP (Fig. 6H–J) around Van (Wick et al., 2003), Zeribar (Stevens et al., 2006), Urmia (Stevens et al., 2012), Mirabad (Bottema, 1986; Stevens et al., 2006) and Almalou Peatland (Chen et al., 2024). As oak-expansion is primarily governed by growing season moisture and summer aridity, the sharp rise in oak pollen during the mid-Holocene is therefore indicative of a shortening of the dry summer season and/or increase in precipitation (most likely during spring) (Djamali et al., 2010; Chen et al., 2024). Further evidence for a mid-Holocene hydroclimate maximum comes from non-pollen hydroclimate records from several other sites, such as Lake Van, Almalou Peatland, Mirabad and the Dead Sea (Fig. 6D–G). The Lake Van Mg/Ca time series shows lowest salinity and higher rainfall between ~6200 and 4000 yrs BP (Fig. 6G), supported by highest lake levels (Wick et al., 2003). In the Levant, Dead Sea level was also higher during the mid-Holocene (Fig. 6D) (Migowski et al., 2006; Litt et al., 2012). Further to the east at Lake Mirabad, ostracod-inferred lake levels are higher during the mid-Holocene, whereas the period between ~10,000 and 6500 yrs BP was possibly even more arid than the late Holocene (Stevens et al., 2006). This observation is underpinned by elevated Sr/Ca values in lacustrine ostracods from Lake Mirabad, which indicate more concentrated lake water as a result of more arid climate conditions during the early Holocene (Stevens et al., 2006). A hydroclimate optimum between ~7500 and 3000 yrs BP is also indicated by the lipid biomarker record (Fig. 6E) from Almalou Peatland on the western Iranian Plateau (Chen et al., 2024), a timing that is in good agreement with our Shalaii Cave record. Overall, the available non-isotope paleoclimate reconstructions show strong evidence for a mid-Holocene hydroclimatic optimum, although there are slight differences in the timing and duration of this period across SW-Asia.

A key-question is which synoptic features were responsible for more arid conditions during the early Holocene and the mid-Holocene hydroclimate optimum in SW-Asia? At present, evidence is mounting that changes in the seasonality of rainfall and/or duration of the dry summer season play a pivotal role during the Holocene. One possible explanation is the monsoon-desert mechanism (Rodwell and Hoskins, 1996), which describes the remote impact of the Indian monsoon on summer aridity in the Mediterranean and SW-Asia. Ascending air in the Indian monsoon domain in summer induces a Rossby-wave pattern to the west and subsidence of warm and dry air over the Mediterranean and SW-Asia. This subsidence suppresses upward motion in the atmosphere and precipitation. Thus, summer aridity over the eastern Mediterranean and SW-Asia is closely related to duration and intensity of the Indian summer monsoon, whereas an earlier onset and stronger monsoon would enhance summer aridity and reduce the duration of the spring rainfall season throughout SW-Asia. Furthermore, the monsoon desert mechanism in combination with higher summer insolation during the early Holocene can amplify summer aridity even further by increasing evapotranspiration (Tzedakis et al., 2009). Thus, the remote impact of the Indian summer monsoon on the length of the rainy and dry season over SW Asia would lead to a change in the seasonality of precipitation, in this case from a winter-dominated precipitation regime during the early Holocene into a regime dominated by both winter and spring precipitation since the middle Holocene (Stevens et al., 2001, 2006). This shift would have reduced the contribution of isotopically more positive spring precipitation to groundwater recharge above Shalaii Cave and explain a proportion of the observed millennial trends in the SHC-03 $\delta^{18}O_{ca}$ and other isotope records in SW Asia (Fig. 5).

Furthermore, the strength and spatial extension of Arabian anticyclone (or Arabian subtropical anticyclone) are additional crucial factors controlling the amount of precipitation in Iraq and SW Asia respectively. Meteorological observations show that years with a shorter rainfall period concur with an earlier northward movement of the Arabian anticyclone in spring (Mohammadi et al., 2021). Such an earlier establishment of the Arabian anticyclone in the region would block the mid-latitudinal rain bearing systems over Iraq and adjacent regions. This mechanism would be consistent with a suggested earlier northward shift of the westerly storm tracks in spring reduced water vapour transport and rainfall during the spring season along the Zagros Mountains (Stevens et al., 2006). The importance of the Arabian anticyclone for spring precipitation throughout SW-Asia is also revealed by climate model simulations. Using the PMIP4 model simulations, Chen et al. (2024) found evidence for a weaker Arabian anticyclone in response to lower spring insolation during the mid-Holocene compared to today (Fig. 7A and B), which also promoted the influx of moisture from the Red and Arabian Sea into SW Asia. Based on the PMIP4 models, Chen et al. (2024) suggested that a more southerly location of the subtropical high during the mid-Holocene resulted in a shortening of the dry summer season in SW-Asia. Lowest spring insolation weakened the intensity of the spring Arabian anticyclone resulted in a higher amount of spring precipitation. Furthermore, the PMIP4 model simulations suggest that the most significant reduction in precipitation from the mid-Holocene to the pre-industrial period (PI) is associated with a decrease in the amount of spring precipitation in SW-Asia. During the mid-Holocene, the Indian summer monsoon and subsidence (desert-monsoon mechanism) was weaker compared to the early Holocene (Fig. 7) and summer aridity was lower, also because summer insolation and therefore thermal heating

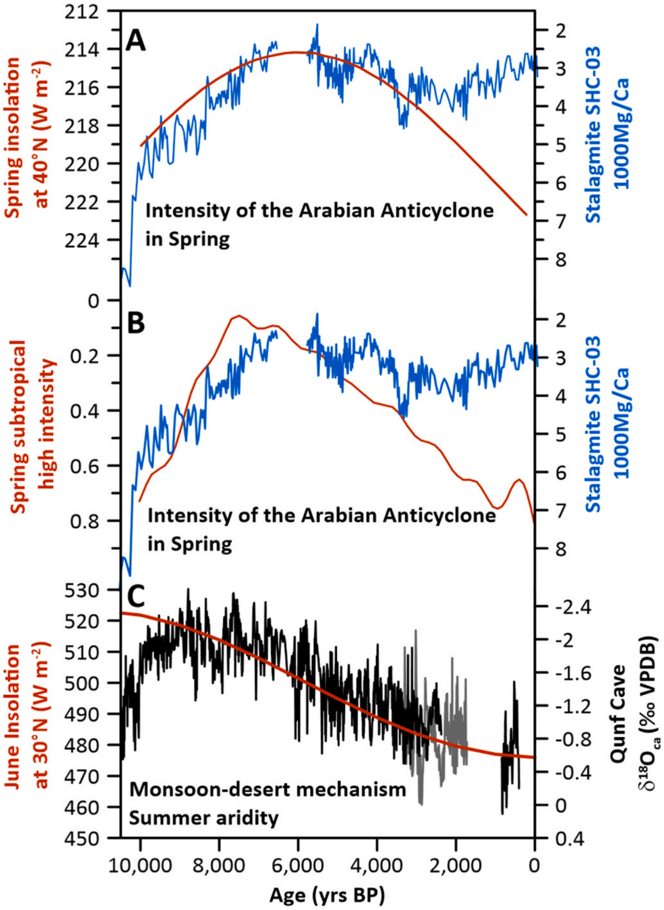

Fig. 7. **(A)** Spring insolation (red line) at 40°N in comparison to the Shalaii Cave Mg/Ca record. **(B)** Simulated spring subtropical (Arabian anticyclone) high intensity (red line) in SW-Asia according to Chen et al. (2024) in comparison to the Shalaii Cave Mg/Ca record. **(C)** The Qunf Cave Indian summer monsoon record from Oman obtain from stalagmites Q5 (black curve) and Q10 (grey-curve) (Fleitmann et al., 2003, 2007, 2022; Tian et al., 2023) in comparison to June insolation (red line). (For interpretation of the references to colour in this figure legend, the reader is referred to the Web version of this article.)

was lower. We therefore suggest that all relevant forcing factors (weaker spring and summer solar insolation) and synoptic circulation patterns varied in concert with respect to spring precipitation. However, the late Holocene hydroclimate change in Iraq and parts of SW-Asia appears to be disconnected from spring insolation forcing and the intensity of the spring subtropical high, as precipitation remains fairly high compared to increasing spring solar insolation and modelled subtropical high intensity (Fig. 7A and B). This decoupling during the late Holocene could possibly be explained by the continuous weakening of the Indian summer monsoon (Fleitmann et al., 2007, 2022; Tian et al., 2023) and concomitant reduction in subsidence over SW-Asia (weakening of the desert-monsoon mechanism) and summer aridity (Fig. 7C). Reduced summer insolation (Fig. 7C) is most likely an additional factor contributing to a lowering of summer aridity. This would have reduced evaporative loss of water during summer and may have counterbalanced any decreases in spring rainfall. It is also possible that a threshold was reached when colder summer temperatures due to reduced summer insolation reduced evaporative loss in Iraq and SW-Asia respectively. Thus lower summer temperatures compromised the reduction of spring precipitation, through the temperature-hydroclimate relationship. However, further data are required to verify our assumption.

Finally, the slow inundation of the Persian Gulf during the early Holocene is rarely considered as an additional factor contributing to the mid-Holocene hydroclimatic optimum. Shorelines and a sea surface area similar to today were reached around 6000 yrs BP (Lambeck, 1996) (Fig. 1A). This would have had an additional effect on spring rainfall as the Persian Gulf is an important moisture source for spring as rainfall which is associated with highly energetic mesoscale convective systems, which can contribute a large proportion of total annual rainfall (Evans and Smith, 2006).

However, we must acknowledge that numerous uncertainties remain. Firstly, the late Holocene hydroclimate evolution appears to be decoupled from spring summer insolation and simulated spring Arabian anticyclone intensity. The ultimate reason for this remains ambiguous. Secondly, changes in the amount of winter and spring rainfall could play an additional role, but we are currently lacking records which can provide more specific information on changes in the amount of autumn, winter and spring rainfall during the Holocene period. Clearly, further studies focusing on the seasonality of rainfall in SW Asia are urgently needed. Thirdly, more highly-resolved regional climate model simulations could help to investigate the evolution of certain synoptic features (e.g., Arabian anticyclone) and storm track trajectories. Overall, much research remains to be done in many regions in SW Asia in order to understand the spatio-temporal hydroclimatic changes.

6. Conclusions

Overall, the new multi-proxy Shalaii Cave record provides additional evidence for a mid-Holocene hydroclimatic optimum in SW-Asia, in agreement with other non-isotopic records from SW-Asia. The millennial-scale trend in oxygen records cannot be explained by changes in the amount of precipitation and a paradigm shift is urgently needed. However, this is only true for the overall Holocene trend and multi-decadal to decadal-scale changes in $\delta^{18}O_{ca}$ are largely influenced by the amount and seasonality effects (e.g., Flohr et al., 2017; Sinha et al., 2019). There is also strong evidence that changes in the seasonal distribution of precipitation occurred during the mid-Holocene hydroclimate optimum, viz. an increase in the amount of spring rainfall and a shorter dry summer season. This assumption is supported by the rapid deciduous oak expansion and reduction of PCP in stalagmite SHC-03 trace element profiles from ~7000 yrs BP onward (Fig. 4B), as a shorter dry summer season would minimize the influence of PCP on Mg and Sr.

In summary, the combined influence of the Arabian anticyclone, Indian summer monsoon (monsoon-desert mechanism) and inundation of the Persian Gulf were most likely the key-elements for the mid-Holocene hydroclimate optimum. However, we do not fully understand to what extent changes in the amount of autumn and winter precipitation contributed to the observed hydroclimate changes and more research is required to shed further light on changes in the seasonality of precipitation in SW-Asia during the Holocene period.

Data availability

Data are available from https://www.ncei.noaa.gov/products/paleoclimatology.

Author contribution

Dominik Fleitmann: conceptualisation; methodology; investigation; formal analysis; writing – initial draft; writing – reviewing and editing, Supervision. Matthew Bosomworth: investigation; data collection; writing – reviewing and editing. Diary Ali Mohammed Amin Al-Manmi: data and sample collection; cave monitoring; reviewing and editing; Melanie J. Leng: methodology; investigation; writing – reviewing and editing; Diane Sahy: investigation; data collection, writing – reviewing and editing; Karen Radner: sample collection, reviewing and editing. Alistair Morgan: sampling, reviewing and editing. Alistair W.G. Pike: data collection; reviewing and editing. Mark Altaweel: sample collection, writing, reviewing and editing.

Funding

This work was supported by the Natural Environmental Research Council, UK (grant IP-1753-1117) and AHRC South, West and Wales Doctoral Training Partnership (grant AH/L503939/1). Further funding is provided by the Swiss National Science Foundation (grant 10000157) and the University of Basel.

Declaration of competing interest

The authors declare that they have no known competing financial interests or personal relationships that could have appeared to influence the work reported in this paper.

The author is an Editorial Board Member/Editor-in-Chief/Associate Editor/Guest Editor for *Quaternary Science Reviews* and was not involved in the editorial review or the decision to publish this article.

Acknowledgements

M.A. and K.R. gratefully acknowledge the decade-long logistical and administrative support of Kamal Rasheed Raheem, then head of the Sulaymaniyah Directorate of Antiquities and Heritage, and his team, on which they heavily relied since they first began to explore the caves in Sulaymaniyah Province in 2012. M.B. acknowledges analytical support by Dr. Matt Cooper, Hilary Sloane and Anne Dudley. M.B. and D.F. would like to thank Dr. Wendy Matthews and Prof. Dr. Roger Matthews for their support at the University of Reading, UK.

Appendix A. Supplementary data

Supplementary data to this article can be found online at https://doi.org/10.1016/j.quascirev.2025.109286.

Data availability

A link to the data and/or code is provided as part of this submission.

References

Almogi-Labin, A., Bar-Matthews, M., Shriki, D., Kolosovsky, E., Paterne, M., Schilman, B., Ayalon, A., Aizenshtat, Z., Matthews, A., 2009. Climatic variability during the last similar to 90 ka of the southern and northern Levantine Basin as evident from marine records and speleothems. Quat. Sci. Rev. 28, 2882–2896.

Amin Al-Manmi, D.A.M., Ismaeel, S.B., Altaweel, M., 2019. Reconstruction of palaeoclimate in Shalaii cave, SE of Sangaw, kurdistan province of Iraq. Palaeogeogr. Palaeoclimatol. Palaeoecol. 524, 262–272.

Andrews, J.E., Carolin, S.A., Peckover, E.N., Marca, A., Al-Omari, S., Rowe, P.J., 2020. Holocene stable isotope record of insolation and rapid climate change in a stalagmite from the Zagros of Iran. Quat. Sci. Rev. 241.

Arz, H.W., Lamy, F., Patzold, J., Muller, P.J., Prins, M., 2003. Mediterranean moisture source for an early-Holocene humid period in the northern Red Sea. Science 300, 118–121.

Barlow, M., Zaitchik, B., Paz, S., Black, E., Evans, J., Hoell, A., 2016. A review of drought in the middle east and Southwest Asia. J. Climate 29, 8547–8574.

Bar-Matthews, M., Ayalon, A., Gilmour, M., Matthews, A., Hawkesworth, C.J., 2003. Sea-land oxygen isotopic relationships from planktonic foraminifera and speleothems in the Eastern Mediterranean region and their implication for paleorainfall during interglacial intervals. Geochem. Cosmochim. Acta 67, 3181–3199.

Bottema, S., 1986. A late quaternary pollen diagram from Lake Urmia (Northwestern Iran). Rev. Palaeobot. Palynol. 47, 241–247, 252-261.

Bowen, G.J., 2020. The online isotopes in precipitation calculator version 3.2. https://wateriso.utah.edu/waterisotopes/pages/data_access/oipc.html.

Breitenbach, S.F.M., Rehfeld, K., Goswami, B., Baldini, J.U.L., Ridley, H.E., Kennett, D.J., Prufer, K.M., Aquino, V.V., Asmerom, Y., Polyak, V.J., Cheng, H., Kurths, J., Marwan, N., 2012. COnstructing proxy records from age models (COPRA). Clim. Past 8, 1765–1779.

Carolin, S.A., Walker, R.T., Day, C.C., Ersek, V., Sloan, R.A., Dee, M.W., Talebian, M., Henderson, G.M., 2018. Precise timing of abrupt increase in dust activity in the Middle East coincident with 4.2 ka social change. Proc. Natl. Acad. Sci. U. S. A. 116, 67–72.

Chen, S., Chen, J., Ding, G., Ma, S., Ji, P., Zhou, A., Wu, D., Khormali, F., Hou, J., Chen, F., 2024. Dipole pattern of Holocene hydroclimate variations across the Asian drylands: critical evidence from west Asia. J. Geophys. Res. Atmos. 129.

Cheng, H., Edwards, R.L., Shen, C.C., Polyak, V.J., Asmerom, Y., Woodhead, J., Hellstrom, J., Wang, Y.J., Kong, X.G., Spotl, C., Wang, X.F., Alexander, E.C., 2013. Improvements in Th-230 dating, Th-230 and U-234 half-life values, and U-Th isotopic measurements by multi-collector inductively coupled plasma mass spectrometry. Earth Planet Sci. Lett. 371, 82–91.

Cheng, H., Sinha, A., Verheyden, S., Nader, F.H., Li, X.L., Zhang, P.Z., Yin, J.J., Yi, L., Peng, Y.B., Rao, Z.G., Ning, Y.F., Edwards, R.L., 2015. The climate variability in northern Levant over the past 20,000 years. Geophys. Res. Lett. 42, 8641–8650.

Crémière, A., Lepland, A., Chand, S., Sahy, D., Condon, D.J., Noble, S.R., Martma, T., Thorsnes, T., Sauer, S., Brunstad, H., 2016. Timescales of methane seepage on the Norwegian margin following collapse of the Scandinavian Ice Sheet. Nat. Commun. 7, 11509.

Davis, B.A.S., Brewer, S., Stevenson, A.C., Guiot, J., 2003. The temperature of Europe during the Holocene reconstructed from pollen data. Quat. Sci. Rev. 22, 1701–1716.

deMenocal, P., Ortiz, J., Guilderson, T., Adkins, J., Sarnthein, M., Baker, L., Yarusinsky, M., 2000. Abrupt onset and termination of the African Humid Period: rapid climate responses to gradual insolation forcing. Quat. Sci. Rev. 19, 347–361.

de Vries, A.J., Feldstein, S.B., Riemer, M., Tyrlis, E., Sprenger, M., Baumgart, M., Fnais, M., Lelieveld, J., 2016. Dynamics of tropical-extratropical interactions and extreme precipitation events in Saudi Arabia in autumn, winter and spring. Q. J. R. Meteorol. Soc. 142, 1862–1880.

Develle, A.L., Herreros, J., Vidal, L., Sursock, A., Gasse, F., 2010. Controlling factors on a paleo-lake oxygen isotope record (Yammouneh, Lebanon) since the Last Glacial Maximum. Quat. Sci. Rev. 29, 865–886.

Djamali, M., Akhani, H., Andrieu-Ponel, V., Braconnot, P., Brewer, S., de Beaulieu, J.L., Fleitmann, D., Fleury, J., Gasse, F., Guibal, F., Jackson, S.T., Lézine, A.M., Médail, F., Ponel, P., Roberts, N., Stevens, L., 2010. Indian Summer Monsoon variations could have affected the early-Holocene woodland expansion in the Near East. Holocene 20, 813–820.

Edwards, R.L., Chen, J.H., Wasserburg, G.J., 1987. U-238 U-234-Th-230-Th-232 systematics and the precise measurement of time over the past 500000 years. Earth Planet Sci. Lett. 81, 175–192.

Evans, J.P., Smith, R.B., 2006. Water vapor transport and the production of precipitation in the eastern fertile crescent. J. Hydrometeorol. 7, 1295–1307.

Fairchild, I.J., Smith, C.L., Baker, A., Fuller, L., Spotl, C., Mattey, D., McDermott, F., Eimp, 2006. Modification and preservation of environmental signals in speleothems. Earth Sci. Rev. 75, 105–153.

Fleitmann, D., Burns, S.J., Mudelsee, M., Neff, U., Kramers, J., Mangini, A., Matter, A., 2003. Holocene forcing of the Indian monsoon recorded in a stalagmite from Southern Oman. Science 300, 1737–1739.

Finné, M., Holmgren, K., Sundqvist, H.S., Weiberg, E., Lindblom, M., 2011. Climate in the eastern Mediterranean, and adjacent regions, during the past 6000 years - a review. J. Archaeol. Sci. 38, 3153–3173.

Fleitmann, D., Burns, S.J., Mangini, A., Mudelsee, M., Kramers, J., Villa, I., Neff, U., Al-Subbary, A.A., Buettner, A., Hippler, D., Matter, A., 2007. Holocene ITCZ and Indian monsoon dynamics recorded in stalagmites from Oman and Yemen (Socotra). Quat. Sci. Rev. 26, 170–188.

Fleitmann, D., Haldon, J., Bradley, R.S., Burns, S.J., Cheng, H., Edwards, R.L., Raible, C. C., Jacobson, M., Matter, A., 2022. Droughts and societal change: the environmental context for the emergence of Islam in late Antique Arabia. Science 376, 1317. +.

Flohr, P., Fleitmann, D., Zorita, E., Sadekov, A., Cheng, H., Bosomworth, M., Edwards, L., Matthews, W., Matthews, R., 2017. Late Holocene droughts in the Fertile Crescent recorded in a speleothem from northern Iraq. Geophys. Res. Lett. 44, 1528–1536.

Fohlmeister, J., Voarintsoa, N.R.G., Lechleitner, F.A., Boyd, M., Brandtstätter, S., Jacobson, M.J., L. Oster, J., 2020. Main controls on the stable carbon isotope composition of speleothems. Geochem. Cosmochim. Acta 279, 67–87.

Frumkin, A., Stein, M., 2004. The Sahara-East Mediterranean dust and climate connection revealed by strontium and uranium isotopes in a Jerusalem speleothem. Earth Planet Sci. Lett. 217, 451–464.

Gasse, F., 2000. Hydrological changes in the African tropics since the last glacial maximum. Quat. Sci. Rev. 19, 189–211.

Goede, A., McCulloch, M., McDermott, F., Hawkesworth, C., 1998. Aeolian contribution to strontium and strontium isotope variations in a Tasmanian speleothem. Chem. Geol. 149, 37–50.

Grant, K.M., Rohling, E.J., Bar-Matthews, M., Ayalon, A., Medina-Elizalde, M., Ramsey, C.B., Satow, C., Roberts, A.P., 2012. Rapid coupling between ice volume and polar temperature over the past 150,000 years. Nature 491, 744–747.

Hennekam, R., Donders, T.H., Zwiep, K., de Lange, G.J., 2015. Integral view of Holocene precipitation and vegetation changes in the Nile catchment area as inferred from its delta sediments. Quat. Sci. Rev. 130, 189–199.

Jones, M.D., Abu-Jaber, N., AlShdaifat, A., Baird, D., Cook, B.I., Cuthbert, M.O., Dean, J. R., Djamali, M., Eastwood, W., Fleitmann, D., Haywood, A., Kwiecien, O., Larsen, J., Maher, L.A., Metcalfe, S.E., Parker, A., Petrie, C.A., Primmer, N., Richter, T., Roberts, N., Roe, J., Tindall, J.C., Ünal-Imer, E., Weeks, L., 2019. 20,000 years of societal vulnerability and adaptation to climate change in southwest Asia. Wires Water 6.

Kharajiany, S.O., 2014. The occurrence of early and middle miocene rocks (Euphrates, Dhiban and Jeribe formations) in Ashdagh mountain, Sangaw area. Iraqi Bull. Geol. Min. 10, 21–39.

Kolodny, Y., Stein, M., Machlus, M., 2005. Sea-rain-lake relation in the last glacial east mediterranean revealed by δ18O-δ13C in lake lisan aragonites. Geochem. Cosmochim. Acta 69, 4045–4060.

Kunkelova, T., Crocker, A.J., Jewell, A.M., Breeze, P.S., Drake, N.A., Cooper, M.J., Milton, J.A., Hennen, M., Shahgedanova, M., Petraglia, M., Wilson, P.A., 2022. Dust sources in Westernmost Asia have a different geochemical fingerprint to those in the Sahara. Quat. Sci. Rev. 294.

Kuper, R., Kröpelin, S., 2006. Climate-controlled Holocene occupation in the sahara: motor of Africa's evolution. Science 313, 803–807.

Lambeck, K., 1996. Shoreline reconstructions for the Persian Gulf since the last glacial maximum. Earth Planet Sci. Lett. 142, 43–57.

Lawrence, D., Philip, G., Gruchy, M.W., 2021. Climate change and early urbanism in Southwest Asia: a review. WIREs Climate Change 13.

Litt, T., Ohlwein, C., Neumann, F.H., Hense, A., Stein, M., 2012. Holocene climate variability in the Levant from the Dead Sea pollen record. Quat. Sci. Rev. 49, 95–105.

Ludwig, K.R., 2003. User's Manual for Isoplot 3.75: A Geochronological Toolkit for Microsoft Excel 5. (Kenneth R Ludwig, 2003).

Marino, G., Rohling, E.J., Sangiorgi, F., Hayes, A., Casford, J.L., Lotter, A.F., Kucera, M., Brinkhuis, H., 2009. Early and middle Holocene in the Aegean Sea: interplay between high and low latitude climate variability. Quat. Sci. Rev. 28, 3246–3262.

Marsh, A., Fleitmann, D., Al-Manmi, D.A.M., Altaweel, M., Wengrow, D., Carter, R., 2018. Mid- to late-Holocene archaeology, environment and climate in the northeast Kurdistan region of Iraq. Holocene 28, 955–967.

McDermott, F., 2004. Palaeo-climate reconstruction from stable isotope variations in speleothems: a review. Quat. Sci. Rev. 23, 901–918.

Migowski, C., Stein, M., Prasad, S., Negendank, J.F.W., Agnon, A., 2006. Holocene climate variability and cultural evolution in the Near East from the Dead Sea sedimentary record. Quat. Res. 66, 421–431.

Mohammadi, Z., Lashkari, H., Mohammadi, M.S., 2021. Synoptic analysis and core situations of Arabian anticyclone in shortest period precipitation in the south and southwest of Iran. Arabian J. Geosci. 14.

Regattieri, E., Forti, L., Drysdale, R.N., Mannella, G., Hellstrom, J.C., Conati Barbaro, C., Bonacossi, D.M., Zerboni, A., 2023. Neolithic hydroclimatic change and water resources exploitation in the Fertile Crescent. Sci. Rep. 13, 45.

Reuter, J., Buenning, N., Yoshimura, K., 2017. Evaluating hydrological influences on mid-latitude δ^{18}Op in the Middle East. Clim. Dyn. 50, 3153–3170.

Roberts, N., Brayshaw, D., Kuzucuoglu, C., Perez, R., Sadori, L., 2011. The mid-Holocene climatic transition in the Mediterranean: causes and consequences. Holocene 21, 3–13.

Rodwell, M.J., Hoskins, B.J., 1996. Monsoons and the dynamics of deserts. Q. J. R. Meteorol. Soc. 122, 1385–1404.

Rohling, E.J., Mayewski, P.A., Abu-Zied, R.H., Casford, J.S.L., Hayes, A., 2002. Holocene atmosphere-ocean interactions: records from Greenland and the Aegean Sea. Clim. Dyn. 18, 587–593.

Rohling, E.J., Marino, G., Grant, K.M., 2015. Mediterranean climate and oceanography, and the periodic development of anoxic events (sapropels). Earth Sci. Rev. 143, 62–97.

Rozanski, K., Araguasaraguas, L., Gonfiantini, R., 1992. Relation between long-term trends of O-18 isotope composition of precipitation and climate. Science 258, 981–985.

Sharifi, A., Pourmand, A., Canuel, E.A., Ferer-Tyler, E., Peterson, L.C., Aichner, B., Feakins, S.J., Daryaee, T., Djamali, M., Beni, A.N., Lahijani, H.A.K., Swart, P.K., 2015. Abrupt climate variability since the last deglaciation based on a high-resolution, multi-proxy peat record from NW Iran: the hand that rocked the Cradle of Civilization? Quat. Sci. Rev. 123, 215–230.

Sharifi, A., Murphy, L.N., Pourmand, A., Clement, A.C., Canuel, E.A., Naderi Beni, A.A.K., Lahijani, H., Delanghe, D., Ahmady-Birgani, H., 2018. Early-Holocene greening of the Afro-Asian dust belt changed sources of mineral dust in West Asia. Earth Planet Sci. Lett. 481, 30–40.

Sinha, A., Kathayat, G., Weiss, H., Li, H.Y., Cheng, H., Reuter, J., Schneider, A.W., Berkelhammer, M., Adali, S.F., Stott, L.D., Edwards, R.L., 2019. Role of climate in the rise and fall of the Neo-Assyrian Empire. Sci. Adv. 5.

Stevens, L.R., Wright, H.E., Ito, E., 2001. Proposed changes in seasonality of climate during the lateglacial and Holocene at Lake Zeribar, Iran. Holocene 11, 747–755.

Stevens, L.R., Ito, E., Schwalb, A., Wright, H.E., 2006. Timing of atmospheric precipitation in the Zagros Mountains inferred from a multi-proxy record from Lake Mirabad, Iran. Quat. Res. 66, 494–500.

Stevens, L.R., Djamali, M., Andrieu-Ponel, V., de Beaulieu, J.L., 2012. Hydroclimatic variations over the last two glacial/interglacial cycles at Lake Urmia, Iran. J. Paleolimnol. 47, 645–660.

Tian, Y., Fleitmann, D., Zhang, Q., Sha, L.J., Wassenburg, J.A., Axelsson, J., Zhang, H.W., Li, X.L., Hu, J., Li, H.Y., Zhao, L., Cai, Y.J., Ning, Y.F., Cheng, H., 2023. Holocene climate change in southern Oman deciphered by speleothem records and climate model simulations. Nat. Commun. 14.

Tremaine, D.M., Froelich, P.N., Wang, Y., 2011. Speleothem calcite farmed in situ: modern calibration of delta(18)O and delta(13)C paleoclimate proxies in a continuously-monitored natural cave system. Geochem. Cosmochim. Acta 75, 4929–4950.

Tzedakis, P.C., Palike, H., Roucoux, K.H., de Abreu, L., 2009. Atmospheric methane, southern European vegetation and low-mid latitude links on orbital and millennial timescales. Earth Planet Sci. Lett. 277, 307–317.

Utida, G., Cruz, F.W., Santos, R.V., Sawakuchi, A.O., Wang, H., Pessenda, L.C.R., Novello, V.F., Vuille, M., Strauss, A.M., Borella, A.C., Stríkis, N.M., Guedes, C.C.F., Dias De Andrade, F.R., Zhang, H., Cheng, H., Edwards, R.L., 2020. Climate changes in Northeastern Brazil from deglacial to Meghalayan periods and related environmental impacts. Quat. Sci. Rev. 250.

van Oldenborgh, G.J., 2016. KNMI climate explorer [Available at: https://climexp.knmi.nl. (Accessed 1 March 2023).

Wassenburg, J.A., Riechelmann, S., Schröder-Ritzrau, A., Riechelmann, D.F.C., Richter, D.K., Immenhauser, A., Terente, M., Constantin, S., Hachenberg, A., Hansen, M., Scholz, D., 2020. Calcite Mg and Sr partition coefficients in cave environments: implications for interpreting prior calcite precipitation in speleothems. Geochem. Cosmochim. Acta 269, 581–596.

Weiss, H., Courty, M.A., Wetterstrom, W., Guichard, F., Senior, L., Meadow, R., Curnow, A., 1993. The genesis and collapse of 3rd millennium North mesopotamian civilization. Science 261, 995–1004.

Wick, L., Lemcke, G., Sturm, M., 2003. Evidence of Lateglacial and Holocene climatic change and human impact in eastern Anatolia: high-resolution pollen, charcoal, isotopic and geochemical records from the laminated sediments of Lake Van, Turkey. Holocene 13, 665–675.

Xoplaki, E., Gonzalez-Rouco, J.F., Luterbacher, J., Wanner, H., 2004. Wet season Mediterranean precipitation variability: influence of large-scale dynamics and trends. Clim. Dyn. 23, 63–78.